Ultra-fast High-temperature Sintering of Strontium Titanate

Tarini Prasad Mishra[a*], Shufan Wang[b], Christian Lenser[a], Dylan Jennings[a], Moritz Kindelmann[a], Wolfgang Rheinheimer[a], Christoph Broeckmann[b, c], Martin Bram[a, d], Olivier Guillon[a, e, f]

[a] *Forschungszentrum Jülich GmbH, Institute of Energy and Climate Research: Materials Synthesis and Processing (IEK-1), 52425, Jülich, Germany*
[b] *Institute of Applied Powder Metallurgy and Ceramics at RWTH Aachen e.V. (IAPK), Augustinerbach 4, 52062 Aachen, Germany*
[c] *Institute for Materials Applications in Mechanical Engineering (IWM), RWTH Aachen University, Augustinerbach 4, 52062 Aachen, Germany*
[d] *Ruhr-Universität Bochum, Institut für Werkstoffe, Universitätsstraße 150, 44801 Bochum, Germany*
[e] *RWTH Aachen University, Institute of Mineral Engineering, 52064 Aachen, Germany*
[f] *Jülich Aachen Research Alliance: JARA-Energy, Jülich 52425, Germany*

Tel.: +49 2461 61-8058
Fax: + 49 2461 61-5700

[*]*Email address: t.mishra@fz-juelich.de (Tarini Prasad Mishra)*

ABSTRACT

Ultrafast High-temperature Sintering (UHS) is a novel sintering process enabling extremely high heating rates by direct contact of sample to electrically heated thin carbon strips. Using strontium titanate as a model system, the densification behavior by UHS was investigated. Controlled experiments via maximum current limitation were used to study the influence of the applied current on the degree of densification and resulting final grain size. Simulations by Finite Element Modeling (FEM) allow estimating the sample temperature reached during UHS, which is in good agreement with the experimental data. Moreover, the FEM simulations show a self-stabilization of the sample temperature by thermal radiation. UHS results suggest that rapid densification can be achieved with an extremely high heating rate. The microstructure of the undoped strontium titanate samples shows exaggerated grain growth and pore-boundary separation, which results in pore entrapment inside grains. The addition of 2 mol% iron in strontium titanate is beneficial by limiting the grain growth during the UHS sintering cycle. Uniform densification and grain growth in the sample is consequently observed. Scanning transmission electron microscopy/energy dispersive x-ray spectroscopy (STEM/EDS) is utilized to analyze grain boundary segregation. Measurement of the electrical conductivity of the UHS sintered samples by impedance spectroscopy suggest that rapid densification by UHS enables full access to the functional properties of strontium titanate as compared to the conventionally sintered material.

KEYWORDS

Ultrafast High-temperature Sintering (UHS), Strontium titanate ($SrTiO_3$), Fast firing, Grain growth, Electric Current Assisted Sintering (ECAS), FEM simulation, Electrical conductivity

1. Introduction

Fabrication of ceramic materials utilizes thermal energy to consolidate loose powders into a bulk solid is a process known as sintering [1]. Traditionally, the primary sintering parameters for densification and grain growth are the temperature and heating time. Recent technological advancements in many industries demand high performance sintered products with novel properties. Additionally, industries seek to process materials with increased energy efficiency by reducing the sintering temperature and heating time. Thus, the limitations of conventional sintering methods are overcome by addition of other process control variables like pressure [2,3], sintering aids [4,5], electric field/current [6–9] and others. The additional degrees of freedom enable to densify ceramics at significantly reduced processing costs and energy. In some of these techniques, the possibility of tailoring the microstructures and properties bears immense potential for industrial applications [10–13].

Electric Field/Current Assisted Sintering (ECAS) processes can lower the sintering temperature and enhance the sintering rate of ceramics [14,15]. Field Assisted Sintering Technology/Spark Plasma Sintering (FAST/SPS) [16,17], and microwave sintering [18] are two methods which have long been used for this purpose. More recently, flash sintering was discovered in 2010, whereby zirconia was sintered to almost full density at a furnace temperature of 850 ^{o}C in < 5s by applying electric fields of ~100 V cm^{-1} directly to the specimen [19]. Since then, it has been shown that flash sintering allows the densification of many oxides and even ceramics of complex compositions [8,20–23]. The most recent work has led to further simplification in the processing of complex ceramics with functional properties by reactive flash sintering [24,25], where powders of elemental oxides are mixed and processed concurrently into single-phased, dense polycrystals. Technological limitations of the flash sintering process with respect to the geometry and shape, the need for electrical contacts, the degree of hot-spot generation, electrochemical reactions, and inhomogeneous densification complicate upscaling of the process [14,26,27]. Recent studies have shown a combination of flash sintering with a more conventional FAST/SPS to densify materials and components at a larger scale, introduced as Flash Spark Plasma Sintering (FSPS) [28,29].

In 2020, a novel sintering technique was introduced by Wang et. al., which was named Ultra-fast High-temperature Sintering (UHS) by the authors [30]. UHS enabled synthesis and sintering of oxide powders in just 10 s without preheating a furnace. The UHS process utilizes electric currents to rapidly heat graphite felts by Joule heating at an extremely high heating rate of 10^4–10^5 °C/min to a maximum temperature of up to 3000° C in inert atmosphere. The green body, irrespective of its shape, is placed between two heated graphite felts and is heated through radiation and thermal conduction [31]. The enhanced densification achieved during UHS is believed to be due to the rapid heating rate [32]. Similarly, Todd et al. hypothesized that in flash sintering the ultra-fast heating rate – one of the main characteristics of flash sintering – causes rapid densification [33]. Even in conventional sintering, rapid thermal heating, also known as fast firing, has been shown to result in an enhanced densification with fine-grained microstructure [8,33–35].

The enhanced densification that is observed during fast firing and other high heating rate sintering processes is likely attributed to the short heating time to the high temperatures, where densification mechanisms predominate over the coarsening [36]. Garcia et al. studied fast firing of fine alumina powder and suggested that transient stresses caused by constrained sintering during fast firing play a

very important role in the acceleration of densification to a dense, fine-grained microstructure [37]. To the contrary, Morgan and Yust [38] investigated the sintering rate of thoria powder compacts under fast firing conditions, and observed that the increase in densification rate was much greater than the corresponding increase in the diffusion coefficient of the slower diffusing species. They explained their observation in terms of material transport by dislocation movement or plastic flow. In a recent study, Rheinheimer et al. [39] observed a high dislocation density of up to 10^{14} m^{-2} in strontium titanate after flash sintering, while almost no dislocations were found after conventional sintering. They concluded the enhanced densification observed in flash sintering could be related to the occurrence of plastic flow. Nevertheless, the underlying mechanism responsible for the enhanced densification during fast firing methods and specifically, the UHS technique is still elusive. Moreover, it is important to point out that the ultra-fast heating rate could adversely retard the densification rate in such a way that premature pore closure, gas entrapment and rapid grain growth could arise in the sample [40].

In the present study, the densification behavior and grain growth of undoped strontium titanate and 2 mol% iron-doped strontium titanate by Ultra-fast High temperature Sintering (UHS) was investigated. Doping of strontium titanate with various metal oxides can be used to control diffusion and grain growth during sintering, as demonstrated previously [41,42]. In this study, iron doping will be utilized to investigate its impact on sintering and microstructure evolution. Conventional sintering of undoped and iron doped strontium titanate shows the decelerating influence of iron dopants on the densification and grain growth behavior [43]. Similar results were obtained for flash sintering [44,45]. After sintering, samples were characterized with respect to the degree of densification and their average grain size. Scanning TEM/energy dispersive x-ray spectroscopy (STEM/EDS) analysis was performed to analyze grain boundary segregation in both the doped and undoped samples. To further understand the grain and grain-boundary effects in these ceramics, the temperature and frequency dependence of the electrical properties at high temperatures have been studied using electrochemical impedance spectroscopy (EIS). The frequency-dependent electrical properties are correlated with microstructural changes using appropriate equivalent circuits that match the observed electrical response in complex impedance spectrum.

2. Experimental procedure

2.1. Starting powder and sample preparation

The synthesis of the starting powders i.e., (i) undoped strontium titanate (STO) and (ii) 2 mol% iron-doped strontium titanate ($SrTi_{0.98}Fe_{0.02}O_{3-\delta}$) is reported elsewhere [43,46,47]. The particle size distribution was measured with the laser diffraction method (LA-950-V2, Horiba Ltd., Tokyo, Japan) resulting in a size distribution of STO and FeSTO of d_{10}=0.69 µm, d_{50}=1.65 µm, and d_{90}=3.93 µm and d_{10}=0.38 µm, d_{50}=1.33 µm, and d_{90}=5.51 µm respectively. The STO starting powder had a unimodal distribution, whereas the FeSTO powder had a bimodal distribution, suggesting the presence of some agglomerates, as shown in Fig. 1.

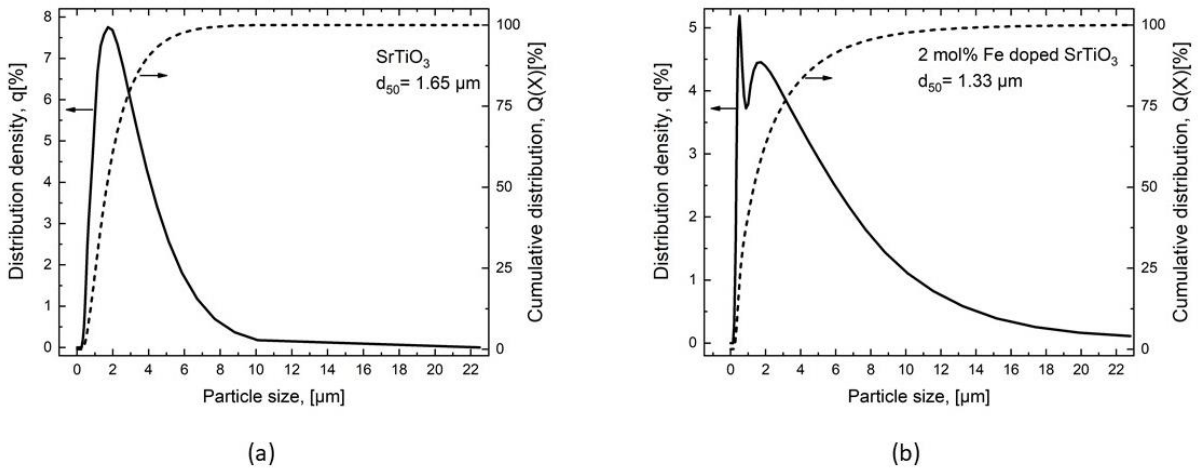

Fig.1. Average particle size distribution: (a) Undoped strontium titanate and (b) Fe-doped strontium titanate.

The powder morphology was observed by SEM, and was isotropic for STO while the FeSTO powder particles show a slightly plate-like shape. The SEM micrographs of the starting powders are reported elsewhere [43]. The elemental concentration and purity of the starting powders was characterized by inductively coupled plasma optical emission spectroscopy (ICP-OES), using a Thermo Scientific iCAP7600 spectrometer with optical scale and CID semi-conductor detector. The mass percentage of the elements in the starting powder is summarized in the supplementary Table 1.

The starting powder was uniaxially pressed in a cylindrical-shaped die with a pressure of 120 MPa and thereafter compacted with a cold isostatic press at a pressure of 300 MPa. The pellet-shaped samples had a diameter of 8 mm and a height of 1±0.15 mm. The amount of powder used for these specimens was 0.15±0.02 g. The relative density of the green pellets was approximately 56-60% as measured geometrically.

2.2. Ultra-fast High temperature sintering (UHS)

A custom-made UHS set-up was used for the experiment as shown in Fig. 2. Two copper electrodes were used as electrodes and contacted to the carbon felt. The UHS setup was operated with an AC/DC power source (TruPlasma Bipolar Series 4000, Trumpf Hüttinger). The UHS setup was placed in a vacuum chamber to achieve an oxygen-lean atmosphere to prevent the carbon felt from oxidizing at high temperatures. Furthermore, the use of vacuum atmosphere in contrast to inert atmospheres minimized the heat loss from the carbon felts. The pellet-shaped samples were pressed with diameter of 8 mm and thickness of 1-1.5 mm uniaxially at 50 MPa and cold-isostatically at 300 MPa for 2 minutes.

After the vacuum was achieved (< 0.2 mbar), the DC electric current (5 A - 25 A) was applied to the carbon felt by metallic copper electrodes, resulting in a very fast heating of the carbon felt due to Joule heating. After the desired maximum current was reached, it was held for 10 s. The power source was subsequently switched off, which resulted in a rapid cooling of the sample. Due to the very high heating rates, the sample temperature could not be measured adequately and unfortunately remains inaccessible in this experiment. The dimension of the carbon felt used in this study was approximately 40 mm in length (between two copper electrode), 9.5 mm in width and 4 mm in thickness.

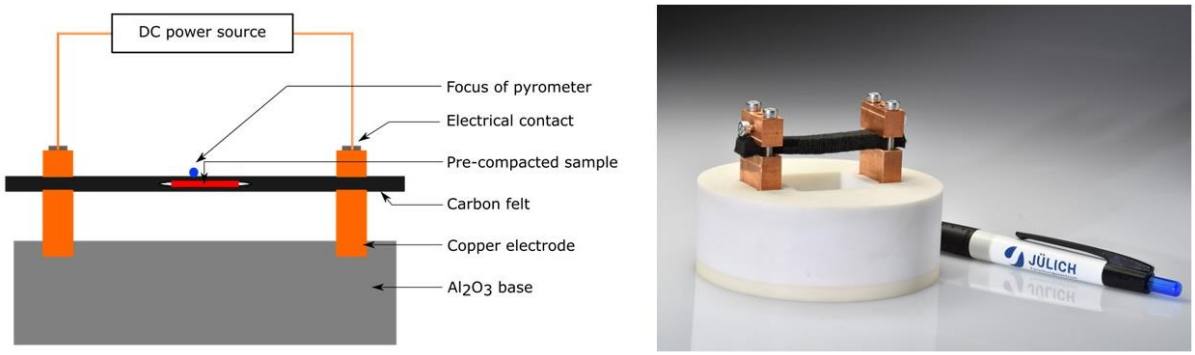

(a) (b)

Fig. 2. (a) Schematic diagram of Ultrafast High-temperature Sintering device and (b) photo of the custom made UHS apparatus that was used in this study

2.3. Modelling and Simulation

To determine the temperature distribution in the samples during UHS, a coupled thermal-electrical model has been built in the commercial Finite Element Method (FEM) software ABAQUS/Standard (v14, Simulia, Dassault Systèmes). The model includes the copper electrodes, the carbon felt, and the $SrTiO_3$ sample as shown in Figure 2. The electrical conductivity of the carbon felt was experimentally measured using test runs without any sample at the maximum currents ranging from 5 to 24 A. In addition, the temperature-dependent thermal conductivity of the Sigratherm® GFA5 carbon felt was taken from [48]. The specific heat capacity of the carbon felt was set the same as the dense graphite from [49] due to its negligible influence on the simulation results. As for the copper and $SrTiO_3$, the thermal conductivity and the specific heat were taken from the literature [50–53]. To ensure that a specific amount of current flows through the graphite felt in the simulation, a surface current density was defined at the left side of the contact surface between the electrode and the carbon felt, see Figure 2 (a). Meanwhile, the contact surface at the right side was kept at a electrical potential of 0 V as boundary condition. Heat was generated inside the carbon felt due to Joule heating and was transferred to the $SrTiO_3$ sample and the electrodes by thermal conduction. Since the carbon felt was stretched during the experiments, the pressure exists continuously at the contact surface between the carbon felt and the electrode/sample. In this case, the thermal contact resistance between them is insignificant and therefore not considered in the model. In vacuum condition, surface radiation of the carbon felt accounts for the majority of the heat loss during UHS. The emissivity of the carbon felt and the copper electrodes used in this study was set to be 0.9 and 0.49, respectively [54,55].

For the verification of the simulation results, the temperatures in the centre of both the inner and the top surface of the carbon felt were experimentally measured. A pyrometer was used for the temperature measurement on the top surface of the carbon felt, as shown in Fig 2 (a). For the inner surface of the carbon felt, a K-type thermocouple was inserted inside the felt (similar to the position of pre-compacted sample) to measure the temperatures at low currents (5 to 8 A), while metal or alloy wires were put inside the carbon felt for UHS at high currents (12 and 16 A). During the measurements, Al_2O_3 protection tubes were adopted for insulation of the thermocouple or the wires from the carbon felt. The UHS processes were stopped after 5 minutes to ensure that the recorded temperature was stabilized. For the maximum currents at 12 A and 16 A, the temperature range was determined according to the melting points T_m of the nickel-chromium (90% Ni-10% Cr) wire (T_m= 1420°C) and the platinum (Pt) wire (T_m= 1768°C). It was found that the Ni-Cr wire melted and the Pt wire remained intact at 12 A, while both wires were melted at 16 A. The temperature inside the carbon felt during UHS at 12 A was then estimated to be between 1420°C and 1768°C, and the temperature at 16 A was above 1768°C. The simulation results of the temperature were extracted from the model at the

positions corresponding to the measurement points and their results were compared. With the validated thermal-electrical model the temperatures of the $SrTiO_3$ samples were predicted at the maximum currents ranging from 16 to 24 A.

2.4. Sample characterization

The final relative density of the sintered samples was measured by the Archimedes' principle in water. The conventional densification behavior of the powder was examined in a push rod dilatometer TMA 402 F1 (Netzsch, Germany). The experiments were performed in argon atmosphere with a constant gas flow of 50 ml·min^{-1}. The dilatometer samples (green) were manufactured as mentioned in section 2.1. The cylinder-shaped samples had a diameter of 8 mm, height of 4 to 5 mm and relative density of around 55%. The dilatometer cycle included a heating ramp with 25°C·min^{-1} to 1500 °C, a dwell time at 1500 °C for 1 min and then cooling to room temperature with 5 °C·min^{-1}. Investigation of the microstructure was performed on polished cross-sections in two cutting perpendicular planes. The surfaces were thermally etched at 1250^{o} C for 20 minutes in a conventional muffle furnace, to delineate the grain boundaries. SEM images of the sputter coated (platinum) microstructures were taken by scanning electron microscopy (Zeiss Cross Beam XB540, Carl Zeiss AG, Oberkochen, Germany). Scanning transmission electron microscopy/energy dispersive x-ray spectroscopy (STEM/EDS) was utilized to characterize grain boundary segregation in the doped and undoped samples. (S)TEM analysis was performed using an FEI Tecnai G2 F20 equipped with a high angle energy dispersive X-ray detector. EDS mapping was performed with a pixel size of between 0.67 and 0.75 nm and drift correction activated, though the high levels of drift limited the resolution achievable with EDS maps and line scans. Focused ion beam (FIB) milling was used for STEM sample preparation (FEI Helios NanoLab 460F1).

2.5. Impedance spectroscopy

Impedance spectra in the frequency range of 10^6 – 10^{-1} Hz were recorded using an Alpha-A High performance Frequency Analyzer (Novocontrol Technologies GmbH, Germany) in a tube furnace in air in the temperature range between 200 °C and 800 °C. The spectral quality was evaluated using the Kramers-Kronig transformation, performed with the Lin-KK software tool [56,57]. Pt paste (Heraeus, Germany) was painted onto the samples and sintered at 900 °C for 2 hours in air to ensure good contact to the Pt mesh of the setup. Complex non-linear least squares (CNLS) fitting to an equivalent circuit model was performed with ZView (Scribner Associates Inc, USA). Each contribution in the spectrum was modelled by a parallel circuit of a resistance and a constant phase element (CPE) with the impedance $Z = 1 / (j\omega Q)^{\alpha}$, where Q and α are the CPE parameters and ω is the angular velocity. The conductivity of the grains (σ_g) and grain boundaries (σ_{gb}) was calculated via:

$$\sigma_g = \frac{L}{R_g \cdot A} \quad (1)$$

and

$$\sigma_{gb} = \frac{L}{R_{gb} \cdot A} \cdot \frac{C_g}{C_{gb}} \quad (2)$$

where L is the thickness of the samle, R_g is the grain resistance, and A is the cross-sectional area of the sample. The ratio of the respective pseudocapacitances of the grain and grain boundary impedances, C_g and C_{gb} respectively, was used as a geometrical correction factor to account for the much smaller grain boundary volume. The pseudocapacitance for each CPE was calculated via:

$$C = R^{\frac{1-\alpha}{\alpha}} \cdot Q^{\alpha} \qquad (3)$$

3. Results and Discussion

3.1. Parameters of UHS sintering and temperature evolution

Figure 3 (a) shows the current and voltage profile during the 4 different UHS cycles under vacuum. The maximum current through the carbon felt was achieved immediately after the power source was switched on due to the high electrical conductivity of the felt. Therefore, the maximum temperature of the carbon felt from room temperature is achieved almost instantaneously. Figure 3 (b) shows the maximum power dissipated through the carbon felt as a function of applied current.

One of the biggest challenges in novel electric field assisted sintering technologies is measurement of the sample temperature accurately, primarily due to the very high heating rate. To overcome this challenge, FEM modelling was carried out to estimate the temperature of the carbon felt. Furthermore, the temperature distribution along the carbon felt and the temperature evolution were investigated. The estimated temperature from the simulation results was verified experimentally.

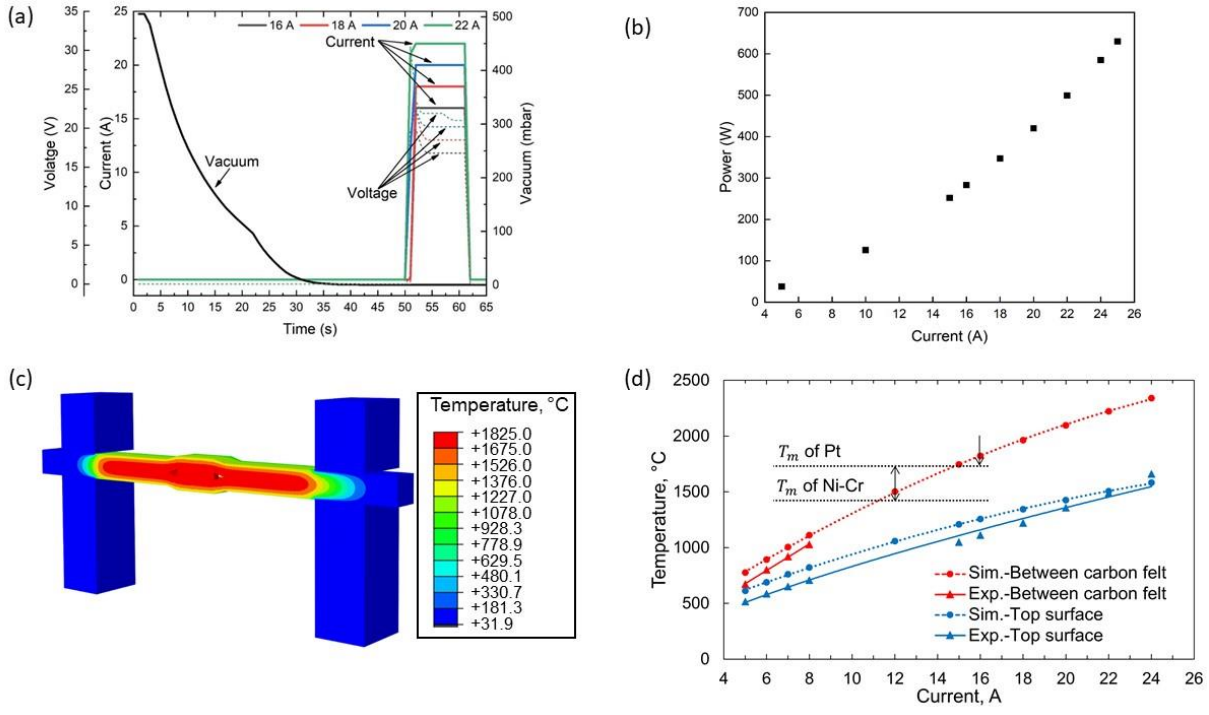

Fig. 3. (a) Electric current and voltage profile of the UHS cycle at 4 different maximum currents, (b) Maximum electrical power as a function of applied current to the carbon felt, (c) UHS set up with simulated temperature gradient at the maximum current of 16 A, cut along the length of the carbon felt at the half-width position and (d) Experimental measurements and simulation results of the temperature between the carbon felt and on the top surface of the felt during UHS at the maximum currents ranging from 5 to 24 A.

The simulation result of the temperature distribution in the UHS setup at 16 A is demonstrated in Figure 3 (c). A large temperature gradient can be observed from the surface to the core of the carbon felt. Nevertheless, a uniform temperature distribution along the path of the current of the carbon felt is observed. The experimental measurements and the simulation results of the temperature are shown in Fig. 3 (d). The temperature estimated by the melted wires were represented as arrows in the graph. It can be seen that both the temperature of the inner and the top surface of the carbon felt increase with higher maximum current. The simulation results correspond well to the experimental measurements. Nevertheless, an overestimation of up to 100°C exists. This deviation may result from the real physical data of the carbon felt. As for the pyrometer measurements, the accuracy of the measurements depends significantly on the precision of the focus. A dispersed focus can lead to an underestimation of the temperature. In summary, the experimental measured temperature is in good agreement with the estimated temperature via the FEM modelling.

3.2. Densification

Cold iso-statically pressed samples were densified by UHS process at different currents ranging from 5 – 25 A. However, the samples densified above 22 A were partially melted at the center. Figure 4 (a) shows images of the UHS samples at two different maximum currents of 18 A and 24 A for 10 s, where it can be observed that the samples UHS at 24 A were partially melted. This suggests that at an applied current of 24 A the temperature of the sample exceeded 2060° C, as the melting point of $SrTiO_3$ is around 2060° C. The modeling of the UHS set-up estimated that in the center of the inner surface of the carbon felt at 24 A, the temperature was approximately 2300° C. Furthermore, the inhomogeneous coloration in the iron -doped sample after UHS suggests a gradient in the distribution of the valence state of the iron in the sample [58]. To understand the distribution of the sample temperature, simulations were performed afterwards with STO samples at the maximum currents of 16 A, 18 A, 20 A, 22 A, and 24 A. It was assumed that there would be negligible difference between the sample temperature in doped and undoped STO samples.

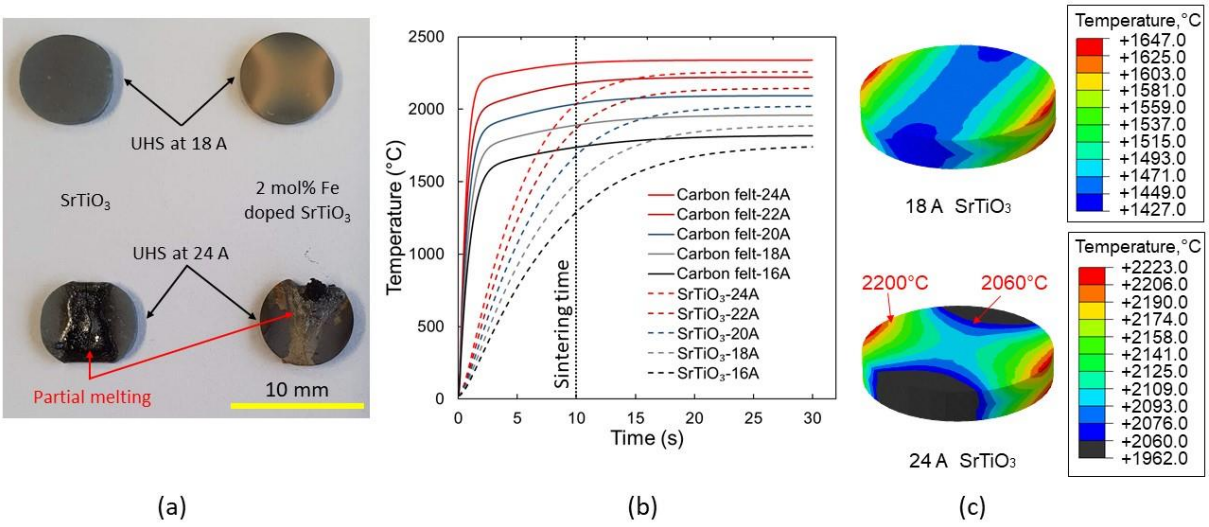

(a) (b) (c)

Fig. 4 (a) Optical images of the UHS sintered samples at different maximum currents. The sample densified by UHS at 24 A has been partially melted, whereas the samples densified by UHS at 18 A are stable, (b) Temperature evolution of the carbon felt (center of the inner surface) and the $SrTiO_3$ samples (averaged over the whole pellet) during UHS at different maximum currents and (c) Simulation results of the UHS sintered $SrTiO_3$ samples at the maximum current of 18 A and 24 A showing a temperature gradient in the samples.

The temperature evolution of the carbon felt and the $SrTiO_3$ samples during UHS at different maximum currents were depicted in Figure 4 (b). The temperature of the carbon felt was extracted in the center of the inner carbon felt, while for $SrTiO_3$ samples the temperatures were averaged over the whole pellet. It can be concluded from the graph that the temperature of the carbon felt reached its highest level within only 3 seconds, while for $SrTiO_3$ samples it took 15-20 seconds for the temperature to stabilize. The dotted line in Figure 4 (b) shows the actual sintering time, which suggest that the samples reached their maximum temperature and then cooled down. Even though the UHS cycles were carried out with a dwell time of 10 s, the samples were sintered without a dwell time. Figure 4 (c) shows the images of the UHS sintered samples at 18 A and 24 A. The original sample (Figure 4, a) sintered at 18 A reveals a slightly distorted shape compared to the original disk. From the simulation results, it can be explained due to the different shrinkage resulting from the inhomogeneous temperature distribution in the sample, as shown in Figure 4 (c). For the UHS sintered sample at 24 A, the partial melting in the middle indicates a temperature above the melting point of SrTiO3 (around 2060°C). Moreover, the top and bottom corners of the pellet completely disappeared due to over-melting. The melted part and the disappeared area of the $SrTiO_3$ sample corresponds to the area above the 2060°C and 2200°C isotherms of the simulation result.

The relative densities of the samples sintered at 16 A for 10 s were 96% and 94% for undoped strontium titanate and 2 mol% iron doped strontium titanate, respectively. As the current was increased to 18 A for 10 s, the relative density reached approximately 98%. The degree of densification remains constant above 18 A for undoped strontium titanate, whereas the relative density of 2 mol% iron doped strontium titanate decreased above 18 A as shown in Figure 5 (a). The SEM micrographs of the samples revealed many micro-cracks along the grain boundaries of the 2 mol% Fe-doped $SrTiO_3$ samples UHS above 18 A (see Figure 7 g and h) leading to the observed decrease of relative density. The micro-cracks in the samples could arise because of the stress generated by the volume change due to the reduction (chemical expansion) of the sample during the UHS process and subsequent oxidation (chemical contraction) of the sample at room temperature, or by thermal stresses triggered by the high heating and cooling rates or rapid densification.

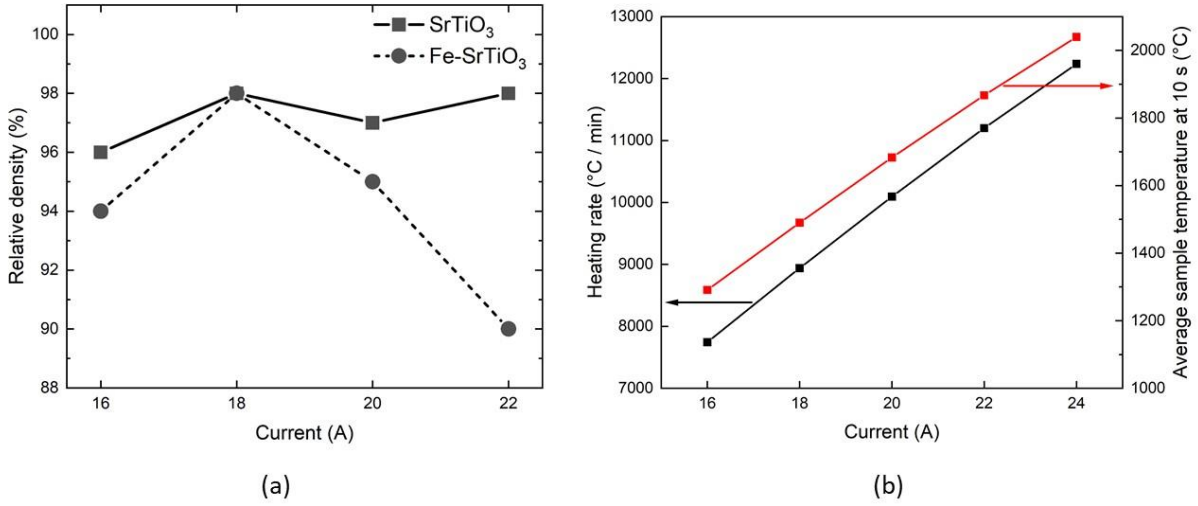

Fig. 5 Relative density of the samples as a function of maximum current, the holding time of at the maximum current was 10 s and (b) Average sample temperature at 10 s and heating rate of the UHS cycle for different currents, the values were extracted from the simulation results

Figure 5 (b) shows the estimated heating rate and the average sample temperature at 10 s for the 4 different UHS cycles with varied currents from the simulation results. These results confirm that the sample experienced an ultra-fast heating rate of 10^4 K/ minute.

The conventional sintering behavior of both materials was investigated by dilatometry in an argon atmosphere to mimic the oxygen-lean atmosphere during UHS cycle. The linear shrinkage of undoped and 2 mol% iron doped strontium titanate as a function of temperature in argon is depicted in supplementary figure S1. As mentioned in the experimental section, the contribution from thermal expansion was subtracted in Figure 6. The onset of densification occurred approximately 100° C lower in iron-doped strontium titanate as compared to undoped-strontium titanate. Nevertheless, the final densification was limited to only a relative density of 77.8% in iron-doped strontium titanate in contrast to a relative density of 96.2% at 1500° C for undoped strontium titanate. A similar observation was reported in the literature [39], where the densification of Fe doped strontium titanate during conventional sintering in air was less than that of undoped strontium titanate. Due to the technical limitations of the dilatometer, the maximum temperature was 1500°C. However, the densification of the samples could be further enhanced by increasing the maximum temperature or dwell time.

As learned from the simulation results, the densification rate that can be achieved by UHS was remarkable compared to the conventional sintering routes. In contrast, at a current of 18 A, all samples can be densified in 10 s nearly to full density irrespective of the doping. From the dilatometer study, the temperature achieved at a current of 18 A should be approximately 1500° C, which was in very good agreement with the estimated sample temperature from the simulation results (1490° C). The remarkably enhanced densification achieved in the UHS process is therefore attributed to the ultra-fast heating rate.

3.3. Microstructure

Figure 6 shows SEM micrographs of the polished and thermally etched cross-sections of UHS sintered pellets at different maximum currents for undoped and 2 mol% doped iron strontium titanate. The micrographs are taken from the middle section of the samples.

The average grain size of undoped strontium titanate increases rapidly with increasing current. The most striking difference in the microstructures was observed between the maximum current of 16 A and 18 A. The UHS sample sintered at 16 A shows limited grain growth and the porosity is still inter-granular. The UHS sample sintered at 18 A has undergone rapid grain growth, and most of the pores are entrapped within the grains. The change in relative density was only 2 % from 16 A to 18 A, whereas the average grain size was increased from 0.6 µm at 16 A to 20 µm at 18 A, by a factor of nearly 35. Furthermore, the grain growth continued as the current was increased to 20 A and 22 A.

The rapid growth in such a short time implies that the grain boundary migration rate is very high above 18 A. The observed pore entrapment inside the individual grains in undoped strontium titanate samples is typical for exaggerated grain growth in general [1] and indicates that the microstructure went through a state of pore-grain boundary separation following the mechanism of pore drag [59,60]. According to the model of pore drag, pores are often separated from the grain boundaries and entrapped inside the rapidly growing grains when the grain boundary migration rate is higher than the pore diffusion rate and the pore drag force is not high enough to hinder grain boundary migration [61]. For pore drag and pore-grain boundary separation, a microstructure development map was introduced in the literature for different mechanisms of densification and grain growth, showing the presence of a pore and grain boundary separation region with respect to relative density and grain size [62].

For strontium titanate, the thermal activation energy is ~8 eV in conventional sintering [63] and ~15eV for grain growth [64]. Accordingly, increasing the temperature favors grain growth over sintering. This

agrees well with the appearance of isolated pores in Fig. 6, i.e. the high temperatures reached during UHS resulted in grain boundary migration rates becoming high enough for pore separation to occur. However, pore-grain boundary separation does not occur for FeSTO. This is likely caused by the reduction of grain growth rates by Fe doping [65,66]. Due to solute drag as Fe segregates to the grain boundaries (see Fig. 8). The slow diffusion of Fe with the moving grain boundary results in a significant reduction of grain growth kinetics, offering a pathway to tailor microstructures during UHS sintering.

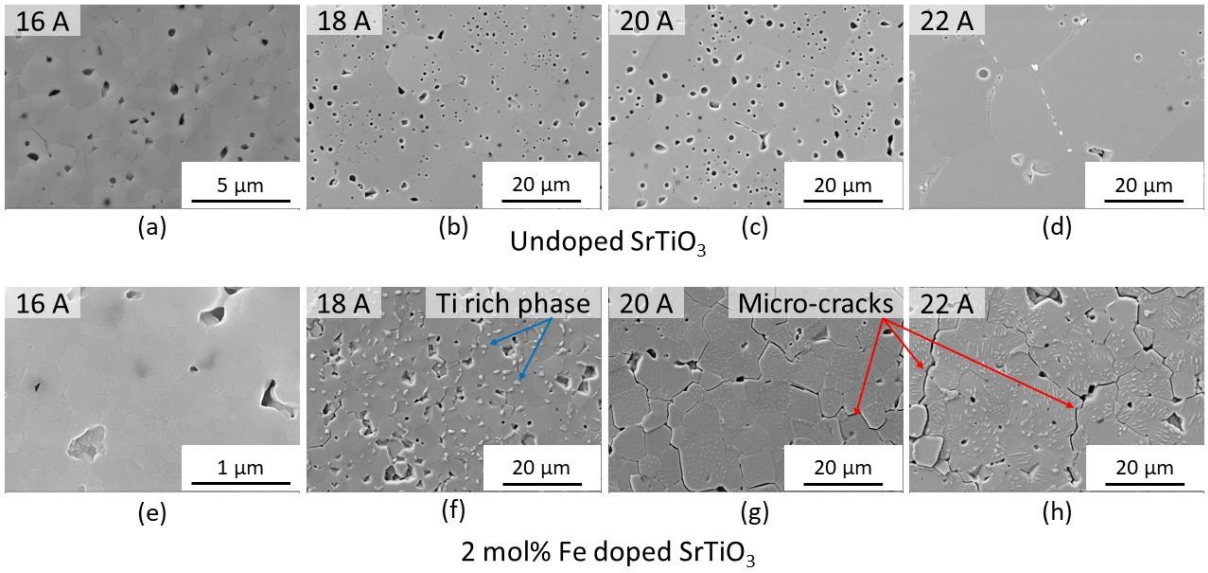

Fig. 6. SEM micrographs of the UHS sintered samples at different maximum currents for 10 s in vacuum chamber, (a-d) undoped strontium titanate and (e-h) 2 mol% iron-doped strontium titanate.

The iron doped sample shows limited grain growth during UHS sintering. The average grain size of the doped $SrTiO_3$ at 16 A was around 140 nm and increased to 4µm, 8 µm and 8.5 µm when UHS-sintered at 18 A, 20 A and 22 A, respectively. The finer microstructure achieved in the 2 mol% iron doped strontium titanate as compared to the undoped strontium titanate agrees well with the previous findings in both conventional sintering and flash sintering [43–45]. Some second phases are evident in the microstructures in Figure 6 and, according to the EDS analysis, are Ti-rich (see supplementary figure 2). As the starting powder is slightly Ti-rich, this is expected and well-documented [67]. Particularly in a reducing atmosphere, the Ti-rich second phase is known to wet the grain boundaries at high temperatures [68], similar to Figure 6 (d).

Figure 7 (a) summarizes average grain size of the UHS sintered samples as a function of maximum applied current. The average grain size was measured at different positions near the middle section of the samples as sketched in Figure 7 (b). In the UHS process, the sample is sandwiched between two carbon felts (see Figure 2), therefore it is likely that the surface of the sample was somewhat hotter

than the middle section of the sample (see the FEM simulation in Fig. 4c).

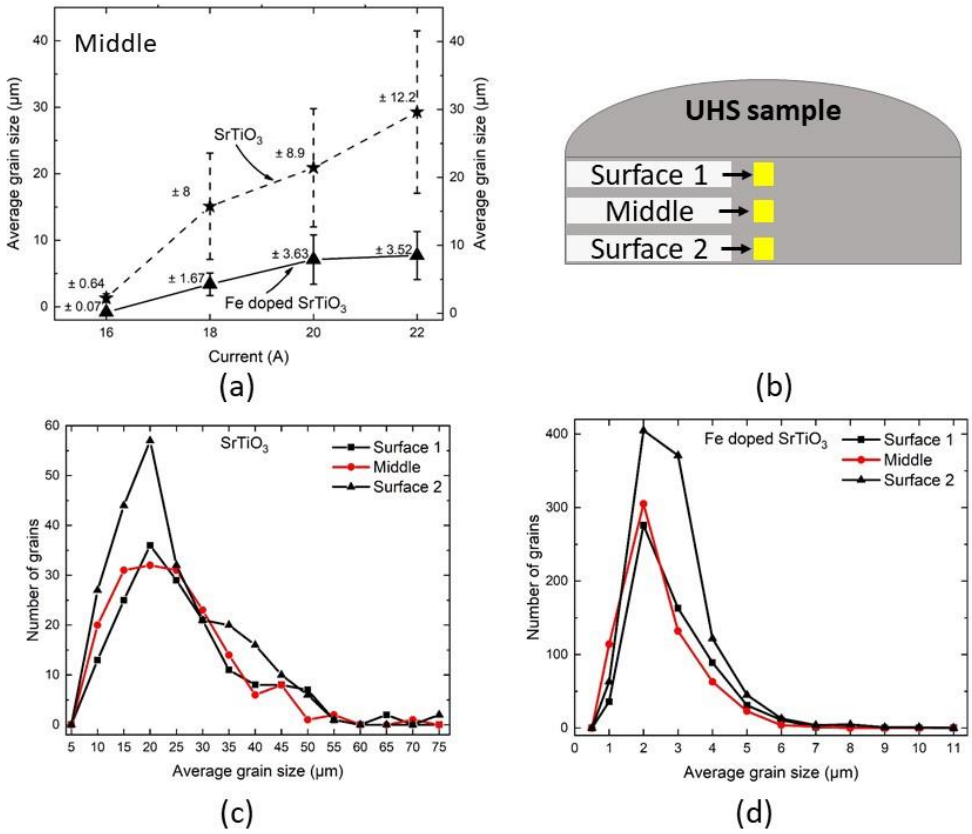

Fig. 7. Grain size statistics of the UHS sintered samples, (a) Average grain size at the middle of the UHS sample as a function of maximum current for both undoped and 2 mol% iron doped SrTiO3, (b) schematics of the samples showing the regions where the grain size analysis was carried out and (c & d) distribution of the grain sizes at three different regions in the samples. Please note that the surface 1 and surface 2 were in direct contact to the carbon felt might experience higher temperature than the middle region of the sample.

Furthermore, the microstructures close to the surface and core (middle) region of the sample were compared, as shown in figure 7 (c and d). It is concluded that the deviation of the grain sizes at different regions of the sample irrespective of the distance to the carbon felt is almost negligible. Therefore, it is safe to assume that the temperature distribution in the sample was relatively homogeneous, primarily because of the moderate sample thickness of approximately 1-1.5 mm. The inhomogeneity in the thermal distribution might increase when comparing to the surface of the sample and the core of the sample when the sample thickness increases further.

3.4. TEM-Characterization of grain boundary regions

(S)TEM investigations were undertaken on both the undoped and the Fe doped strontium titanate samples which were sintered at a current of 18A. Previous studies have identified high dislocation densities in flash sintered STO [39]. However, a TEM investigation of the UHS samples revealed no dislocations in either the undoped or the FeSTO. STEM/EDS mapping was performed to characterize elemental segregation at the grain boundaries (aligned in an edge-on condition) for both samples, as seen in Figure 8.

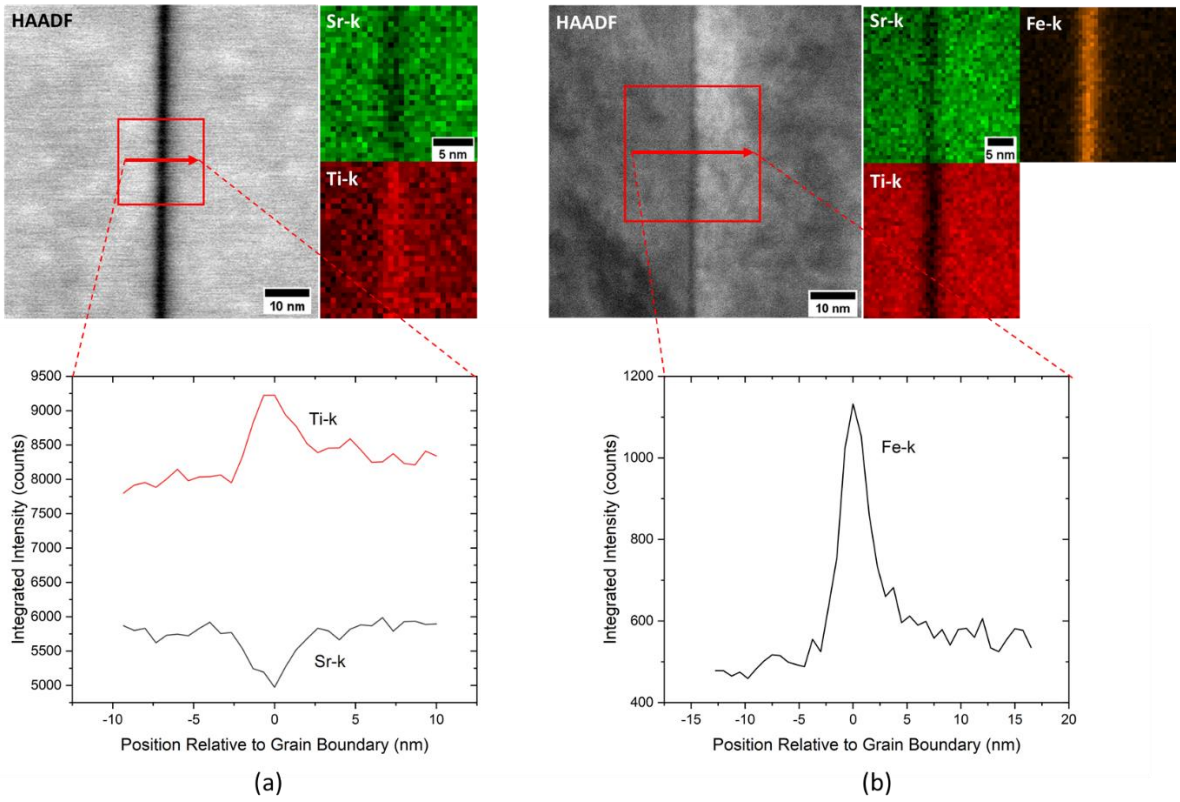

Fig. 8. STEM/EDS analysis of elemental segregation at the grain boundaries. High angular annular dark field (HAADF) image of a grain boundary in (a) undoped STO and (b) Fe doped STO, along with corresponding EDS maps and line scans. Ti excess and strontium deficiency at the boundary is observed in the undoped sample, while Fe segregation is evident in the Fe doped sample.

In the undoped STO sample, Sr deficiency and Ti excess is observed at the grain boundary (Figure 8a), whereas the FeSTO sample shows Fe segregation at the grain boundary, coupled with Ti and Sr deficiency (Figure 8b). The observed segregation is typical to what has been seen in previous studies for conventionally sintered strontium titanate [65,69–72]. Line scans integrated perpendicular to the grain boundary show that the elemental segregation has a width of 3-4 nm in both samples (the width of segregation was taken to be the full width at half maximum of the gaussian fit of the line scan). Grain boundaries in strontium titanate have been found to be rich in oxygen vacancies, creating a space charge that is compensated by corresponding strontium vacancies [70,71], which matches well with the segregation behavior seen here. In the case of FeSTO, Fe (residing on Ti sites in the crystal) segregates to the boundary, resulting in the Fe excess and Ti deficiency that can be observed in Figure 8b. Ti excess is typically expected at STO grain boundaries, but high enough levels of iron doping have been shown to result in Ti deficiency similar to what is detected here [65]. However, Zahler et al., [66] have shown that Ti deficiency is not seen until the Fe dopant level reaches 5% in conventionally sintered STO, indicating that the UHS process results in a slightly different GB chemistry.

The typical space charge concept suggests that segregation will occur in the space charge region near the grain boundary. The segregation in Figure 8 is shown to be only 3-4 nm wide, and is expected to be thinner than this, but instrumentation limitations restricted the ability to be more exact (see section 2.2). This result suggests that the segregation in UHS samples is sharper than for conventionally sintered STO, though further study is required to confirm that differences in segregation are caused by the UHS technique. The differences in grain boundary segregation could be explained by the high temperatures and short sintering times present in the UHS process. It has been shown that the equilibrium space charge width and potential is highly dependent on the temperature [70].

Additionally, full equilibration of the grain boundary chemistry may not occur during the short sintering period, resulting in a non-equilibrium distribution of defects in the grain boundary and space charge region. Understanding the full effects of the UHS process on grain boundary segregation is critical, as a difference in grain boundary chemistry will likely have a significant impact on the electrical properties of the material.

3.5. Electrical conductivity

After sintering with a maximum current of 18 A, samples of STO and FeSTO were investigated with impedance spectroscopy. The distinct discoloration observed after UHS (cf. Figure 4 a) disappeared during the firing process of the Pt electrodes. While the STO sample showed a homogeneous light color after Pt firing, the FeSTO sample was homogeneously dark. The coloration of the FeSTO can be assumed to be due to the Fe^{4+} dopants in the lattice, indicating that both samples were re-oxidized during electrode firing. Interestingly, the Pt electrode adhered well to STO, whereas it delaminated partially from the FeSTO sample.

Figure 9 shows the total, grain and grain boundary conductivity ($\sigma_{tot,}$ σ_{grain} and $\sigma_{GB,}$ respectively) of STO and FeSTO as a function of inverse temperature. The grain and grain boundary conductivity of FeSTO could be only determined below a temperature of 575 °C due to their respective frequency dispersion, whereas the grain and grain boundary conductivity of STO could be determined in the entire investigated temperature range up to 800 °C due to its lower total conductivity. The total conductivity of FeSTO shows an activation energy of E_A = 0.67 eV, which is indicative of primarily ionic conduction [73]. This would be expected for a sample sintered under a moderately low oxygen activity. The activation energy of the STO sample was much higher with E_A = 1.63 eV.

The relative contributions of σ_{grain} and σ_{GB} to σ_{tot} are markedly different for STO and FeSTO. While σ_{grain} and σ_{tot} are almost identical for FeSTO, σ_{tot} is much lower than σ_{grain} for STO. The underlying reason is that the overall resistance is dominated by the grain resistance in FeSTO, whereas it is dominated by the grain boundary resistance in STO (see Figure S2 in the supplementary information). The low grain boundary conductivity of undoped STO is caused by space charge layers: STO is known to have a positive grain boundary core along with a negative space charge layer, overall resulting in a Schottky barrier and a low grain boundary conductivity [74–77]. The decrease in grain boundary resistance in FeSTO is likely associated to the accumulation of Fe-acceptors at the grain boundaries, as evidenced by Figure 8b. Their negative charge decreases the magnitude of the positive grain boundary core charge, resulting in less space charge and a lower Schottky barrier at the grain boundaries [70,78]. As a consequence, the thermal activation of the FeSTO conductivity is determined by the energy barrier for oxygen vacancy hopping in the bulk, whereas the activation of the conductivity of STO is determined by the blocking character of the grain boundaries. As such, this behavior is expected from the examined materials and does not indicate that the used UHS treatment has a pronounced (detrimental) effect on the functionality of the materials examined in this study.

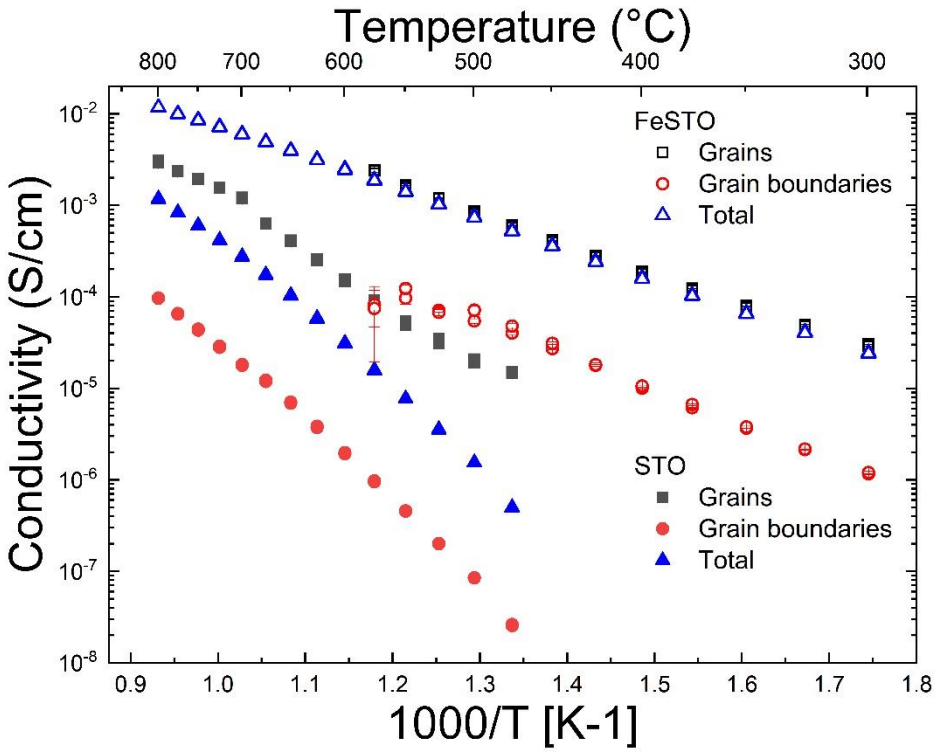

Fig. 9. Conductivity values for the total (triangles), grain (squares) and grain boundary (circles) conductivity of undoped STO (solid symbols) and FeSTO (open symbols) sintered via UHS at a maximum current of 18 A and holding time of 10 s.

4. Discussion

The densification and grain growth achieved by UHS technique is quite remarkable as the process time is as short as a few seconds. The results suggest that the rapid densification can be achieved by sintering at an extremely high heating rate. The rapid densification is likely caused by the extreme heating rate. The driving force for sintering is the reduction of the free surface area of the powder compact and acts in the form of capillarity at the sintering neck [1]. During conventional sintering, very low heating rates result in a long time spent at relatively low temperatures where surface diffusion is the predominant diffusion mechanism [36]. Accordingly, during heating, a large part of the driving force is lost by coarsening, i.e., sintering neck growth, which does not result in any densification. When finally, the sintering temperature is reached and grain boundary and/or volume diffusion become the predominant diffusion mechanism resulting in densification, the lack of driving force results in very long heating times.

On the other hand, the UHS process minimizes the time spent at relatively low temperatures. As such, the loss of driving force by neck growth and coarsening is minimized and the full capillarity is maintained up to high temperatures, where the densification-relevant diffusion mechanisms (i.e. grain boundary and volume diffusion) occur.

The microstructures in Fig. 6 indicate that the relationship between sintering and grain growth is different than in conventional sintering, likely caused by the high activation energy for grain growth compared to sintering. As a result, pores are separated from the grain boundaries in undoped strontium titanate. Fe doping has proven to be adequate to control this effect.

5. Conclusions

In the present work, the densification behavior and grain growth of undoped and 2 mol% iron doped strontium titanate was investigated by novel UHS process. Utilizing direct heating by electrically heated carbon felts allows to achieve an extremely high heating rate of 10^4 K/min and promotes rapid densification and grain growth within seconds. Furthermore, by controlling the electrical current in the graphite heaters, it is possible to control the degree of densification and microstructure of the material.

At a higher applied current, excessive grain growth was observed in undoped strontium titanate, and the pores are entrapped in the grains. The observed pore entrapment in undoped strontium titanate samples can be interpreted by the pore-boundary separation mechanism. This probably decreases the pinning effect of intergranular porosity and therefore allows increased grain boundary migration rates. The excessive grain growth can be controlled by addition of 2 mol% iron in the strontium titanate.

A combination of experimental measurements and FEM modelling was used to determine the temperature distribution in the $SrTiO_3$ samples during UHS. A relatively good agreement between the experimental and numerical results was achieved. The simulation result of the temperature distribution in the UHS sintered $SrTiO_3$ sample at the maximum current of 24 A is able to explain the partial melting of the sample, which proves the reliability of the model to predict the temperature distribution in the samples. The simulation of the thermal evolution of the carbon felt as well as the $SrTiO_3$ samples during UHS at different maximum currents indicates that some time (15-20 s) is needed for the $SrTiO_3$ samples to reach their maximum sintering temperature while the carbon felt can reach this state within seconds. The simulation study showed that during this UHS process, the samples never reached a steady state and the densification was achieved without any dwell time.

(S)TEM investigation of grain boundary segregation shows some differences in the grain boundary chemistry of samples prepared by UHS, likely affecting the measured electrical properties of the materials. The results are in good agreement with the previous findings in conventional free sintering and flash sintering of the same material systems. Detailed investigation of the samples sintered by UHS shows the densification and grain growth to be homogeneous across the specimen.

The UHS technology opens new opportunities in achieving rapid densification by the utilization of electric current. Due to the technical simplicity of the process, it is possible to consolidate materials with different shapes and sizes without any applied pressure. Furthermore, unlike flash sintering where optimum electrical contact remains a challenge for upscaling of the technology, UHS does not have such challenges. Even continuous processes seem possible. Accordingly, UHS bears immense technological potential for various ceramic applications. The current study has proven the quality of the ceramics obtained by UHS.

6. Acknowledgements

The authors would like to thank Ms. Beatrix Göths for the help on acquiring SEM images. The authors acknowledge funding from the Deutsche Forschungsgemeinschaft (DFG) in the framework of the priority program “Manipulation of Matter Controlled by Electric and Magnetic Fields: Towards Novel Synthesis and Processing Routes of Inorganic Materials” (SPP 1959) under the Grant No. “BR 3418/1-2” and “BR 1844/21-2”. WR thanks the DFG for funding within the Emmy Noether program (RH 146-1/1).

6. References

[1] M.N. Rahaman, Sintering of Ceramics, CRC Press, 2007.

[2] R.M. German, Chapter Ten - Sintering With External Pressure, in: R.M. German (Ed.), Sintering: From Empirical Observations to Scientific Principles, Butterworth-Heinemann, Boston, 2014: pp. 305–354. https://doi.org/10.1016/B978-0-12-401682-8.00010-0.

[3] H.V. Atkinson, S. Davies, Fundamental aspects of hot isostatic pressing: An overview, Metall and Mat Trans A. 31 (2000) 2981–3000. https://doi.org/10.1007/s11661-000-0078-2.

[4] K. Watari, H.J. Hwang, M. Toriyama, S. Kanzaki, Effective Sintering Aids for Low-temperature Sintering of AlN Ceramics, Journal of Materials Research. 14 (1999) 14. https://doi.org/10.1557/JMR.1999.0191.

[5] K. Nur, T.P. Mishra, J.G.P. da Silva, J. Gonzalez-Julian, M. Bram, O. Guillon, Influence of powder characteristics on cold sintering of nano-sized ZnO with density above 99 %, Journal of the European Ceramic Society. 41 (2021) 2648–2662. https://doi.org/10.1016/j.jeurceramsoc.2020.11.007.

[6] M. Biesuz, V.M. Sglavo, Flash sintering of ceramics, Journal of the European Ceramic Society. 39 (2019) 115–143. https://doi.org/10.1016/j.jeurceramsoc.2018.08.048.

[7] C.E.J. Dancer, Flash sintering of ceramic materials, Mater. Res. Express. 3 (2016) 102001. https://doi.org/10.1088/2053-1591/3/10/102001.

[8] M.Z. Becker, N. Shomrat, Y. Tsur, Recent Advances in Mechanism Research and Methods for Electric-Field-Assisted Sintering of Ceramics, Advanced Materials. 30 (2018) 1706369. https://doi.org/10.1002/adma.201706369.

[9] T.P. Mishra, R.R.I. Neto, R. Raj, O. Guillon, M. Bram, Current-rate flash sintering of gadolinium doped ceria: Microstructure and Defect generation, Acta Materialia. 189 (2020) 145–153. https://doi.org/10.1016/j.actamat.2020.02.036.

[10] R.K. Bordia, S.-J.L. Kang, E.A. Olevsky, Current understanding and future research directions at the onset of the next century of sintering science and technology, Journal of the American Ceramic Society. 100 (2017) 2314–2352. https://doi.org/10.1111/jace.14919.

[11] E.A. Olevsky, D.V. Dudina, Field-Assisted Sintering: Science and Applications, Springer, 2018.

[12] M. Biesuz, S. Grasso, V.M. Sglavo, What's new in ceramics sintering? A short report on the latest trends and future prospects, Current Opinion in Solid State and Materials Science. 24 (2020) 100868. https://doi.org/10.1016/j.cossms.2020.100868.

[13] O. Guillon, C. Elsässer, O. Gutfleisch, J. Janek, S. Korte-Kerzel, D. Raabe, C.A. Volkert, Manipulation of matter by electric and magnetic fields: Toward novel synthesis and processing routes of inorganic materials, Materials Today. 21 (2018) 527–536. https://doi.org/10.1016/j.mattod.2018.03.026.

[14] M. Bram, A.M. Laptev, T.P. Mishra, K. Nur, M. Kindelmann, M. Ihrig, J.G.P. da Silva, R. Steinert, H.P. Buchkremer, A. Litnovsky, F. Klein, J. Gonzalez-Julian, O. Guillon, Application of Electric Current-Assisted Sintering Techniques for the Processing of Advanced Materials, Advanced Engineering Materials. n/a (n.d.) 2000051. https://doi.org/10.1002/adem.202000051.

[15] S. Grasso, Y. Sakka, G. Maizza, Electric current activated/assisted sintering (ECAS): a review of patents 1906–2008, Science and Technology of Advanced Materials. 10 (2009) 053001. https://doi.org/10.1088/1468-6996/10/5/053001.

[16] O. Guillon, J. Gonzalez-Julian, B. Dargatz, T. Kessel, G. Schierning, J. Räthel, M. Herrmann, Field-Assisted Sintering Technology/Spark Plasma Sintering: Mechanisms, Materials, and Technology Developments, Advanced Engineering Materials. 16 (2014) 830–849. https://doi.org/10.1002/adem.201300409.

[17] T.P. Mishra, A.M. Laptev, M. Ziegner, S.K. Sistla, A. Kaletsch, C. Broeckmann, O. Guillon, M. Bram, Field-Assisted Sintering/Spark Plasma Sintering of Gadolinium-Doped Ceria with Controlled Re-Oxidation for Crack Prevention, Materials. 13 (2020) 3184. https://doi.org/10.3390/ma13143184.
[18] K.E. Haque, Microwave energy for mineral treatment processes—a brief review, International Journal of Mineral Processing. 57 (1999) 1–24. https://doi.org/10.1016/S0301-7516(99)00009-5.
[19] M. Cologna, B. Rashkova, R. Raj, Flash Sintering of Nanograin Zirconia in <5 s at 850°C: Rapid Communications of the American Ceramic Society, Journal of the American Ceramic Society. 93 (2010) 3556–3559. https://doi.org/10.1111/j.1551-2916.2010.04089.x.
[20] R. Raj, Analysis of the Power Density at the Onset of Flash Sintering, Journal of the American Ceramic Society. 99 (2016) 3226–3232. https://doi.org/10.1111/jace.14178.
[21] T.P. Mishra, V. Avila, R.R.I. Neto, M. Bram, O. Guillon, R. Raj, On the role of Debye temperature in the onset of flash in three oxides, Scripta Materialia. 170 (2019) 81–84. https://doi.org/10.1016/j.scriptamat.2019.05.030.
[22] S. Bhandari, T.P. Mishra, O. Guillon, D. Yadav, M. Bram, Accessing the role of Joule heating on densification during flash sintering of YSZ, Scripta Materialia. 211 (2022) 114508. https://doi.org/10.1016/j.scriptamat.2022.114508.
[23] T.P. Mishra, R.R.I. Neto, G. Speranza, A. Quaranta, V.M. Sglavo, R. Raj, O. Guillon, M. Bram, M. Biesuz, Electronic conductivity in gadolinium doped ceria under direct current as a trigger for flash sintering, Scripta Materialia. 179 (2020) 55–60. https://doi.org/10.1016/j.scriptamat.2020.01.007.
[24] S.E. Murray, T.J. Jensen, S.S. Sulekar, Y.-Y. Lin, N.H. Perry, D.P. Shoemaker, Propagation of the contact-driven reduction of Mn2O3 during reactive flash sintering, Journal of the American Ceramic Society. 102 (2019) 7210–7216. https://doi.org/10.1111/jace.16654.
[25] K. Wang, B. Ma, T. Li, C. Xie, Z. Sun, D. Liu, J. Liu, L. An, Fabrication of high-entropy perovskite oxide by reactive flash sintering, Ceramics International. 46 (2020) 18358–18361. https://doi.org/10.1016/j.ceramint.2020.04.060.
[26] T.P. Mishra, C. Lenser, R. Raj, O. Guillon, M. Bram, Development of a processing map for safe flash sintering of gadolinium-doped ceria, Journal of the American Ceramic Society. n/a (n.d.). https://doi.org/10.1111/jace.17847.
[27] G.M. Jones, M. Biesuz, W. Ji, S.F. John, C. Grimley, C. Manière, C.E.J. Dancer, Promoting microstructural homogeneity during flash sintering of ceramics through thermal management, MRS Bulletin. 46 (2021) 59–66. https://doi.org/10.1557/s43577-020-00010-2.
[28] S. Grasso, T. Saunders, H. Porwal, O. Cedillos-Barraza, D.D. Jayaseelan, W.E. Lee, M.J. Reece, Flash Spark Plasma Sintering (FSPS) of Pure ZrB2, Journal of the American Ceramic Society. 97 (2014) 2405–2408. https://doi.org/10.1111/jace.13109.
[29] E.A. Olevsky, S.M. Rolfing, A.L. Maximenko, Flash (Ultra-Rapid) Spark-Plasma Sintering of Silicon Carbide, Scientific Reports. 6 (2016) 33408. https://doi.org/10.1038/srep33408.
[30] C. Wang, W. Ping, Q. Bai, H. Cui, R. Hensleigh, R. Wang, A.H. Brozena, Z. Xu, J. Dai, Y. Pei, C. Zheng, G. Pastel, J. Gao, X. Wang, H. Wang, J.-C. Zhao, B. Yang, X. (Rayne) Zheng, J. Luo, Y. Mo, B. Dunn, L. Hu, A general method to synthesize and sinter bulk ceramics in seconds, Science. 368 (2020) 521–526. https://doi.org/10.1126/science.aaz7681.
[31] M. Ihrig, T.P. Mishra, W.S. Scheld, G. Häuschen, W. Rheinheimer, M. Bram, M. Finsterbusch, O. Guillon, Li7La3Zr2O12 solid electrolyte sintered by the ultrafast high-

temperature method, Journal of the European Ceramic Society. 41 (2021) 6075–6079. https://doi.org/10.1016/j.jeurceramsoc.2021.05.041.
[32] J. Dong, V. Pouchly, M. Biesuz, V. Tyrpekl, M. Vilémová, M. Kermani, M. Reece, C. Hu, S. Grasso, Thermally-insulated ultra-fast high temperature sintering (UHS) of zirconia: A master sintering curve analysis, Scripta Materialia. 203 (2021) 114076. https://doi.org/10.1016/j.scriptamat.2021.114076.
[33] W. Ji, B. Parker, S. Falco, J.Y. Zhang, Z.Y. Fu, R.I. Todd, Ultra-fast firing: Effect of heating rate on sintering of 3YSZ, with and without an electric field, Journal of the European Ceramic Society. 37 (2017) 2547–2551. https://doi.org/10.1016/j.jeurceramsoc.2017.01.033.
[34] D.E. García, D. Hotza, R. Janssen, Building a Sintering Front through Fast Firing, International Journal of Applied Ceramic Technology. 8 (2011) 1486–1493. https://doi.org/10.1111/j.1744-7402.2011.02609.x.
[35] G.J. Pereira, R.H.R. Castro, D.Z. de Florio, E.N.S. Muccillo, D. Gouvêa, Densification and electrical conductivity of fast fired manganese-doped ceria ceramics, Materials Letters. 59 (2005) 1195–1199. https://doi.org/10.1016/j.matlet.2004.12.027.
[36] M.-Y. Chu, M.N. Rahaman, L.C.D. Jonghe, R.J. Brook, Effect of Heating Rate on Sintering and Coarsening, Journal of the American Ceramic Society. 74 (1991) 1217–1225. https://doi.org/10.1111/j.1151-2916.1991.tb04090.x.
[37] D.E. García, J. Seidel, R. Janssen, N. Claussen, Fast firing of alumina, Journal of the European Ceramic Society. 15 (1995) 935–938. https://doi.org/10.1016/0955-2219(95)00071-2.
[38] C.S. Morgan, C.S. Yust, Material transport during sintering of materials with the fluorite structure, Journal of Nuclear Materials. 10 (1963) 182–190. https://doi.org/10.1016/0022-3115(63)90053-9.
[39] W. Rheinheimer, X.L. Phuah, L. Porz, M. Scherer, J. Cho, H. Wang, Does flash sintering involve plastic flow?, Acta Materialia. (2022).
[40] J. Wang, R. Raj, Estimate of the Activation Energies for Boundary Diffusion from Rate-Controlled Sintering of Pure Alumina, and Alumina Doped with Zirconia or Titania, Journal of the American Ceramic Society. 73 (1990) 1172–1175. https://doi.org/10.1111/j.1151-2916.1990.tb05175.x.
[41] K. Maca, V. Pouchlý, K. Bodišová, P. Švančárek, D. Galusek, Densification of fine-grained alumina ceramics doped by magnesia, yttria and zirconia evaluated by two different sintering models, Journal of the European Ceramic Society. 34 (2014) 4363–4372. https://doi.org/10.1016/j.jeurceramsoc.2014.06.030.
[42] S.-J.L. Kang, S.-Y. Ko, S.-Y. Moon, Mixed control of boundary migration and the principle of microstructural evolution, Journal of the Ceramic Society of Japan. 124 (2016) 259–267. https://doi.org/10.2109/jcersj2.15262.
[43] F. Lemke, W. Rheinheimer, M.J. Hoffmann, Sintering and grain growth in $SrTiO_3$: impact of defects on kinetics, Journal of the Ceramic Society of Japan. 124 (2016) 346–353. https://doi.org/10.2109/jcersj2.15265.
[44] F. Lemke, W. Rheinheimer, M.J. Hoffmann, A comparison of power controlled flash sintering and conventional sintering of strontium titanate, Scripta Materialia. 130 (2017) 187–190. https://doi.org/10.1016/j.scriptamat.2016.12.008.
[45] W. Rheinheimer, X.L. Phuah, H. Wang, F. Lemke, M.J. Hoffmann, H. Wang, The role of point defects and defect gradients in flash sintering of perovskite oxides, Acta Materialia. 165 (2019) 398–408. https://doi.org/10.1016/j.actamat.2018.12.007.
[46] M. Bäurer, H. Kungl, M.J. Hoffmann, Influence of Sr/Ti Stoichiometry on the Densification Behavior of Strontium Titanate, Journal of the American Ceramic Society. 92 (2009) 601–606. https://doi.org/10.1111/j.1551-2916.2008.02920.x.

[47] W. Rheinheimer, M. Bäurer, H. Chien, G.S. Rohrer, C.A. Handwerker, J.E. Blendell, M.J. Hoffmann, The equilibrium crystal shape of strontium titanate and its relationship to the grain boundary plane distribution, Acta Materialia. 82 (2015) 32–40. https://doi.org/10.1016/j.actamat.2014.08.065.
[48] P. Morgan, Carbon Fibers and Their Composites, CRC Press, Boca Raton, 2005. https://doi.org/10.1201/9781420028744.
[49] D.R. Gaskell, D.E. Laughlin, Introduction to the thermodynamics of materials, 2018.
[50] C.Y. Ho, R.W. Powell, P.E. Liley, Thermal Conductivity of the Elements, Journal of Physical and Chemical Reference Data. 1 (1972) 279–421. https://doi.org/10.1063/1.3253100.
[51] G.K. White, S.J. Collocott, Heat Capacity of Reference Materials: Cu and W, Journal of Physical and Chemical Reference Data. 13 (1984) 1251–1257. https://doi.org/10.1063/1.555728.
[52] O. Okhay, A. Tkach, Impact of Graphene or Reduced Graphene Oxide on Performance of Thermoelectric Composites, C. 7 (2021) 37. https://doi.org/10.3390/c7020037.
[53] D. de Ligny, P. Richet, High-temperature heat capacity and thermal expansion of ${\mathrm{SrTiO}}_{3}$ and ${\mathrm{SrZrO}}_{3}$ perovskites, Phys. Rev. B. 53 (1996) 3013–3022. https://doi.org/10.1103/PhysRevB.53.3013.
[54] M. Kermani, J. Dong, M. Biesuz, Y. Linx, H. Deng, V.M. Sglavo, M.J. Reece, C. Hu, S. Grasso, Ultrafast high-temperature sintering (UHS) of fine grained α-Al2O3, Journal of the European Ceramic Society. 41 (2021) 6626–6633. https://doi.org/10.1016/j.jeurceramsoc.2021.05.056.
[55] W.R. Wade, W.R. Wade, Langley Aeronaut. Lab. NASA, Technical note 4206 (1958) [AD 153 191], (n.d.).
[56] M. Schönleber, D. Klotz, E. Ivers-Tiffée, A Method for Improving the Robustness of linear Kramers-Kronig Validity Tests, Electrochimica Acta. 131 (2014) 20–27. https://doi.org/10.1016/j.electacta.2014.01.034.
[57] M. Schönleber, E. Ivers-Tiffée, Approximability of impedance spectra by RC elements and implications for impedance analysis, Electrochemistry Communications. 58 (2015) 15–19. https://doi.org/10.1016/j.elecom.2015.05.018.
[58] C. Lenser, A. Kalinko, A. Kuzmin, D. Berzins, J. Purans, K. Szot, R. Waser, R. Dittmann, Spectroscopic study of the electric field induced valence change of Fe-defect centers in SrTiO3, Phys. Chem. Chem. Phys. 13 (2011) 20779–20786. https://doi.org/10.1039/C1CP21973A.
[59] J. Hötzer, V. Rehn, W. Rheinheimer, M.J. Hoffmann, B. Nestler, Phase-field study of pore-grain boundary interaction, Journal of the Ceramic Society of Japan. 124 (2016) 329–339. https://doi.org/10.2109/jcersj2.15266.
[60] V. Rehn, J. Hötzer, W. Rheinheimer, M. Seiz, C. Serr, B. Nestler, Phase-field study of grain growth in porous polycrystals, Acta Materialia. 174 (2019) 439–449. https://doi.org/10.1016/j.actamat.2019.05.059.
[61] R.J. Brook, Pore-Grain Boundary Interactions and Grain Growth, Journal of the American Ceramic Society. 52 (1969) 56–57. https://doi.org/10.1111/j.1151-2916.1969.tb12664.x.
[62] Kang: Sintering: densification, grain growth and... - Google Scholar, (n.d.). https://scholar.google.com/scholar_lookup?title=Sintering%3A%20Densification%2C%20Grain%20Growth%20and%20Microstructures&publication_year=2005&author=S.J.%20Kang (accessed June 4, 2021).
[63] L. Amaral, A.M.R. Senos, P.M. Vilarinho, Sintering kinetic studies in nonstoichiometric strontium titanate ceramics, Materials Research Bulletin. 44 (2009) 263–270. https://doi.org/10.1016/j.materresbull.2008.06.002.

[64] M. Bäurer, D. Weygand, P. Gumbsch, M.J. Hoffmann, Grain growth anomaly in strontium titanate, Scripta Materialia. 61 (2009) 584–587. https://doi.org/10.1016/j.scriptamat.2009.05.028.
[65] K.S.N. Vikrant, W. Rheinheimer, H. Sternlicht, M. Bäurer, R.E. García, Electrochemically-driven abnormal grain growth in ionic ceramics, Acta Materialia. 200 (2020) 727–734. https://doi.org/10.1016/j.actamat.2020.08.027.
[66] M.P. Zhaler, Manuscript in preparation, (2022).
[67] W. Rheinheimer, M. Bäurer, C.A. Handwerker, J.E. Blendell, M.J. Hoffmann, Growth of single crystalline seeds into polycrystalline strontium titanate: Anisotropy of the mobility, intrinsic drag effects and kinetic shape of grain boundaries, Acta Materialia. 95 (2015) 111–123. https://doi.org/10.1016/j.actamat.2015.05.019.
[68] W. Rheinheimer, M. Bäurer, M.J. Hoffmann, A reversible wetting transition in strontium titanate and its influence on grain growth and the grain boundary mobility, Acta Materialia. 101 (2015) 80–89. https://doi.org/10.1016/j.actamat.2015.08.069.
[69] S.-M. Wang, S.-J.L. Kang, Grain Boundary Segregation and High Nonlinear I–V Characteristics in Fe-Added Strontium Titanate, Journal of the American Ceramic Society. 91 (2008) 2617–2622. https://doi.org/10.1111/j.1551-2916.2008.02532.x.
[70] R.A.D. Souza, The formation of equilibrium space-charge zones at grain boundaries in the perovskite oxide SrTiO3, Phys. Chem. Chem. Phys. 11 (2009) 9939–9969. https://doi.org/10.1039/B904100A.
[71] S. von Alfthan, N.A. Benedek, L. Chen, A. Chua, D. Cockayne, K.J. Dudeck, C. Elsässer, M.W. Finnis, C.T. Koch, B. Rahmati, M. Rühle, S.-J. Shih, A.P. Sutton, The Structure of Grain Boundaries in Strontium Titanate: Theory, Simulation, and Electron Microscopy, Annual Review of Materials Research. 40 (2010) 557–599. https://doi.org/10.1146/annurev-matsci-010510-104604.
[72] W. Rheinheimer, J.P. Parras, J.-H. Preusker, R.A. De Souza, M.J. Hoffmann, Grain growth in strontium titanate in electric fields: The impact of space-charge on the grain-boundary mobility, Journal of the American Ceramic Society. 102 (2019) 3779–3790. https://doi.org/10.1111/jace.16217.
[73] D.M. Long, B. Cai, J.N. Baker, P.C. Bowes, T.J.M. Bayer, J.-J. Wang, R. Wang, L.-Q. Chen, C.A. Randall, D.L. Irving, E.C. Dickey, Conductivity of iron-doped strontium titanate in the quenched and degraded states, Journal of the American Ceramic Society. 102 (2019) 3567–3577. https://doi.org/10.1111/jace.16212.
[74] J. Lund, K.S.N. Vikrant, C.M. Bishop, W. Rheinheimer, R.E. García, Thermodynamically consistent variational principles for charged interfaces, Acta Materialia. 205 (2021) 116525. https://doi.org/10.1016/j.actamat.2020.116525.
[75] D.S. Mebane, R.A.D. Souza, A generalised space-charge theory for extended defects in oxygen-ion conducting electrolytes: from dilute to concentrated solid solutions, Energy Environ. Sci. 8 (2015) 2935–2940. https://doi.org/10.1039/C5EE02060C.
[76] Y.-M. Chiang, T. Takagi, Grain-Boundary Chemistry of Barium Titanate and Strontium Titanate: II, Origin of Electrical Barriers in Positive-Temperature-Coefficient Thermistors, Journal of the American Ceramic Society. 73 (1990) 3286–3291. https://doi.org/10.1111/j.1151-2916.1990.tb06451.x.
[77] Y.-M. Chiang, T. Takagi, Grain-Boundary Chemistry of Barium Titanate and Strontium Titanate: I, High-Temperature Equilibrium Space Charge, Journal of the American Ceramic Society. 73 (1990) 3278–3285. https://doi.org/10.1111/j.1151-2916.1990.tb06450.x.
[78] K.S.N. Vikrant, W. Rheinheimer, R.E. García, Electrochemical drag effect on grain boundary motion in ionic ceramics, Npj Comput Mater. 6 (2020) 1–7. https://doi.org/10.1038/s41524-020-00418-z.
[79] R. Raj, Joule heating during flash-sintering, Journal of the European Ceramic Society. 32 (2012) 2293–2301. https://doi.org/10.1016/j.jeurceramsoc.2012.02.030.

Supplementary Information

Supplementary table 1: ICP-OES measurements of undoped strontium titanate and 2 mol% iron doped strontium titanate

	Undoped $SrTiO_3$	**2mol% Fe-$SrTiO_3$**
Element	**[Wt. %]**	**[Wt. %]**
Al	<0,0009	<0,0009
B	<0,1	<0,1
Ba	0.0094	0.00521
Ca	0.0281	0.0282
Co	<0,0006	<0,0006
Cr	0.0015	0.0015
Cu	0.0092	0.0088
Fe	**0.0023**	**1.401**
Hf	0.0029	0.0036
K	<0,004	<0,004
La	0.0093	0.0088
Li	<0,02	<0,02
Mg	<0,002	<0,002
Mn	<0,002	<0,002
Mo	<0,0001	<0,0001
Na	<0,09	<0,09
Ni	<0,001	<0,001
P	<0,005	<0,005
Si	<0,008	<0,008
Sr	**48.5**	**48.5**
Ti	**25.63**	**24.24**
V	<0,003	<0,003
Y	0.0064	0.0096
Zn	<0,002	<0,002
Zr	0.0935	0.147

BBR model:

The BBR model used in this study to estimate the sample temperature is reported elsewhere [79], which is derived from the Stefan-Boltzmann law and modified for the flash experiment condition (Eq. 1).

$$\frac{T}{T_0} = \left[1 + \frac{1000 * W_v}{\sigma T_0^4} \left(\frac{V}{A}\right)\right]^{1/4} \qquad \text{Eq. 1}$$

In Eq. 1, T is the sample temperature (K), T_0 the furnace temperature (K), A is the surface area (mm^2), V is the volume of the sample (mm^3), W_v is the normalized power dissipated in the sample with respect to the volume of the sample (W mm^{-3}), σ = 5.670374419...×10^{-8} W*m^{-2}*K^{-4} is the Stefan–Boltzmann constant and α is a correction factor to account the emissivity of the sample. In the current experiments, the emissivity of carbon felt was assumed to be 1.

The length, width and the thickness of the carbon felt was 4.4 mm, 9.5 mm and 4.2 mm respectively.

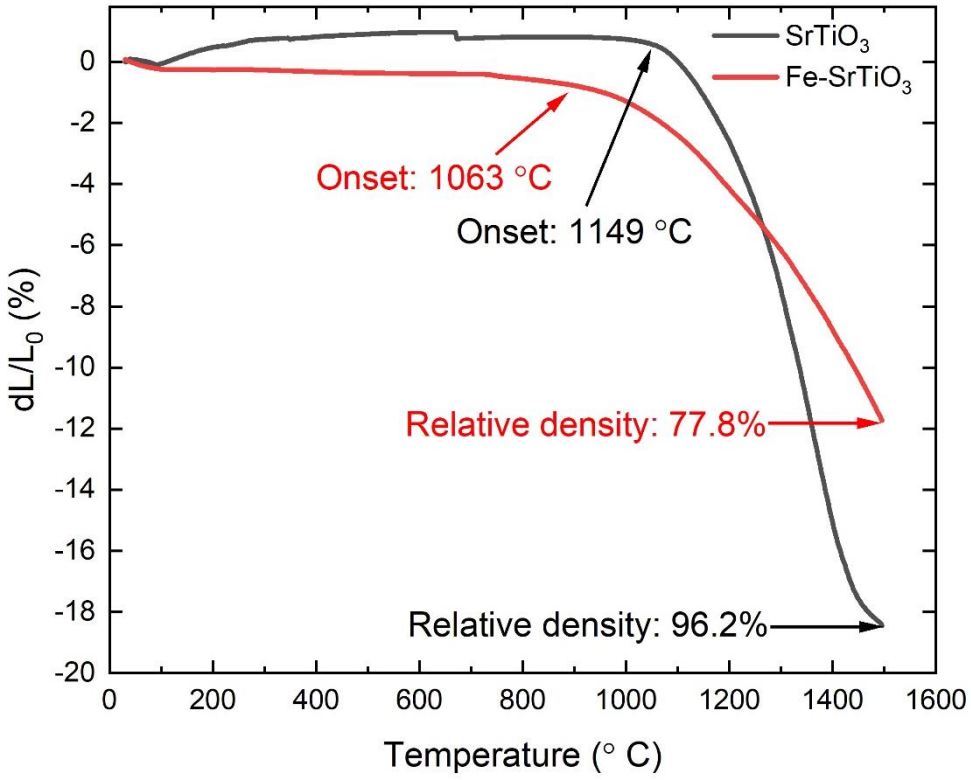

Fig. S1. Uniaxial shrinkage curve from dilatometry of undoped $SrTiO_3$ and 2 mol% Fe doped $SrTiO_3$. Dilatometer parameters: heating rate of 25° C/min, maximum temperature 1500° C, 1 min holding time and in Argon.

EDS elemental mapping:

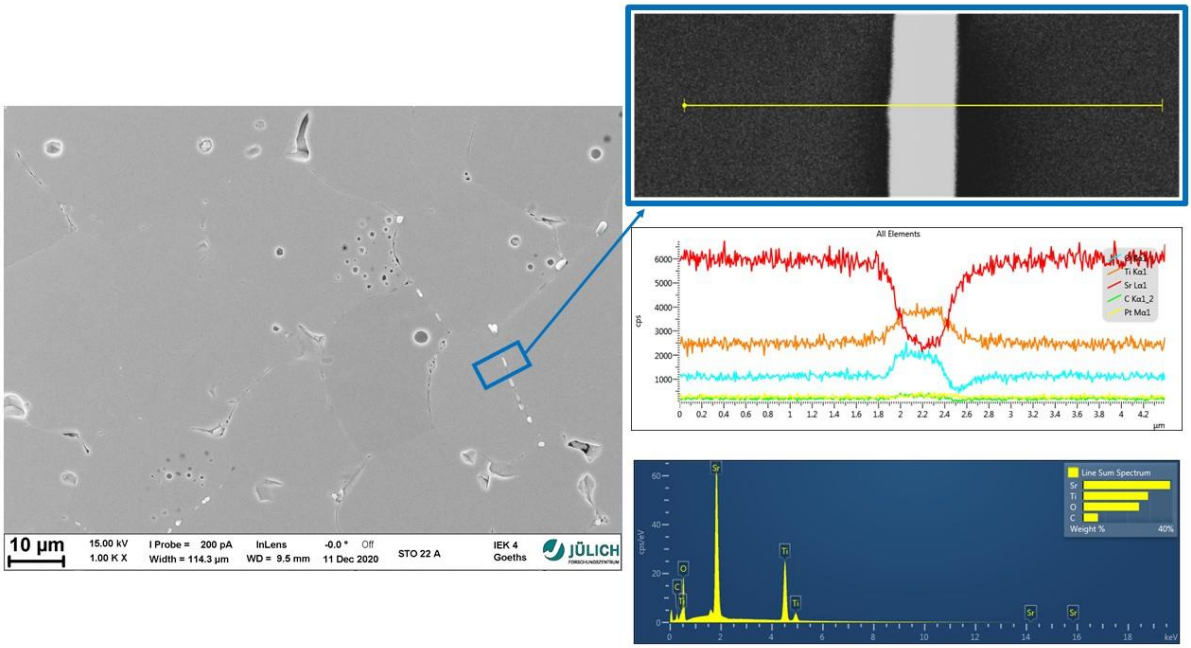

Supplementary Fig. S2. EDS elemental mapping showing the Ti rich phase

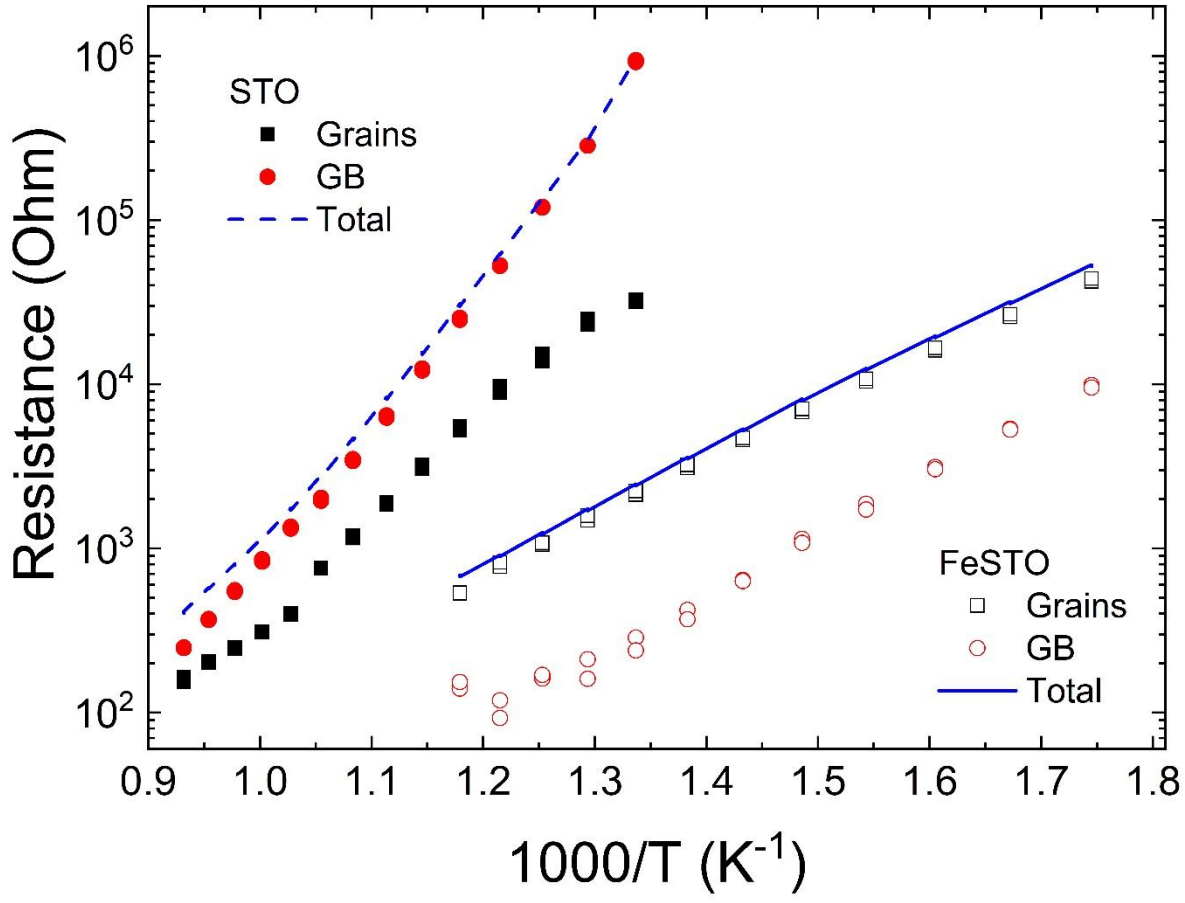

Supplementary Fig. S3: Resistance vs. inverse temperature for grains, grain boundaries and total resistance for STO and FeSTO

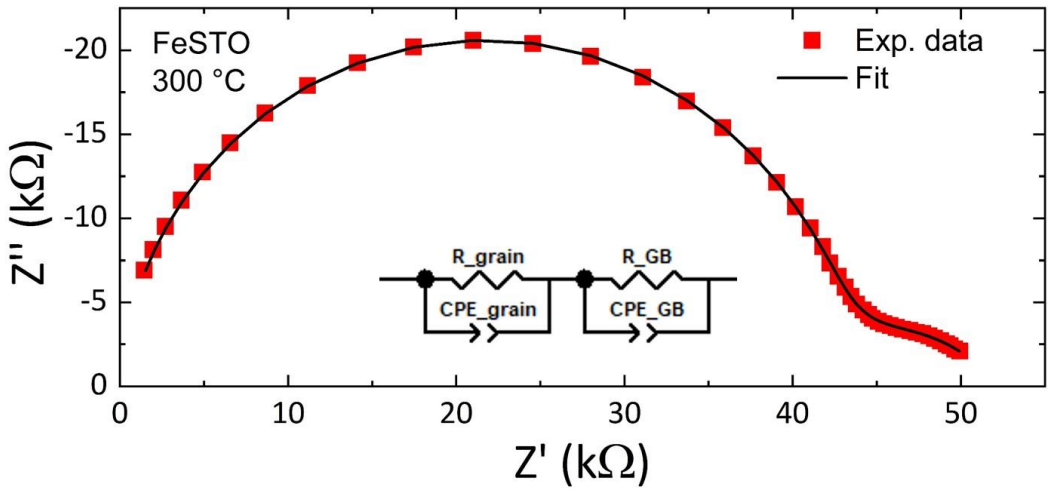

Supplementary Fig. S4: Nyquist plot of an exemplary data set for Fe-doped STO at 300 °C in air. The red squares are the data points, the black line is the fit to the data using the model shown in the inset.